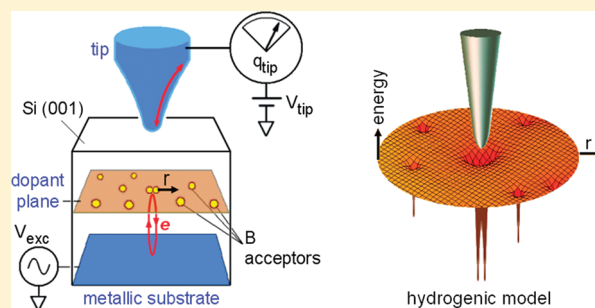


Single-Electron Capacitance Spectroscopy of Individual Dopants in Silicon

M. Gasseller,^{†,‡} M. DeNinno,[†] R. Loo,[‡] J. F. Harrison,[§] M. Caymax,[‡] S. Rogge,^{⊥,||} and S. H. Tessmer^{*,†}[†]Department of Physics and Astronomy, Michigan State University, East Lansing, Michigan 48824, United States[‡]IMEC, Kapeldreef 75, B-3001 Leuven, Belgium[§]Department of Chemistry, Michigan State University, East Lansing, Michigan 48864, United States[⊥]Delft University of Technology, Kavli Institute of Nanoscience, NL-2628 CJ Delft, Netherlands^{||}Centre for Quantum Computation and Communication Technology, School of Physics, The University of New South Wales, Sydney 2052, Australia Supporting Information

ABSTRACT: Motivated by recent transport experiments and proposed atomic-scale semiconductor devices, we present measurements that extend the reach of scanned-probe methods to discern the properties of individual dopants tens of nanometers below the surface of a silicon sample. Using a capacitance-based approach, we have both spatially resolved individual subsurface boron acceptors and detected spectroscopically single holes entering and leaving these minute systems of atoms. A resonance identified as the B^+ state is shown to shift in energy from acceptor to acceptor. We examine this behavior with respect to nearest-neighbor distances. By directly measuring the quantum levels and testing the effect of dopant–dopant interactions, this method represents a valuable tool for the development of future atomic-scale semiconductor devices.

KEYWORDS: Subsurface dopants, dopant molecules, single-electron tunneling, capacitance, scanning probe microscopy



As the size of conventional semiconductor components is reduced to nanometer scales, the exponential Moore's-Law improvement in the performance is determined by ever fewer numbers of dopants. The ultimate goal is to develop devices based on manipulating the charge and spin of individual dopant atoms.^{1–3} Elucidating the electronic structure of these minute systems is a difficult technical challenge.

In a recent study, Kuljanishvili and co-workers performed single-electron capacitance measurements of subsurface silicon donors in gallium-arsenide using subsurface charge accumulation (SCA) imaging.^{4,5} The method essentially probed the quantum states of clusters of donors by measuring the electron addition energies, the energy at which the system will accommodate an additional charge. This study did not have sufficient spatial resolution to resolve the charging of individual subsurface dopants. In another recent study, Caro and co-workers applied resonant tunneling spectroscopy to study the quantum states of boron acceptors in silicon.⁶ A clear conductance resonance was observed and shown to be consistent with tunneling through the B^+ state, for which two holes are bound to the boron atom. With regard to the energy of the resonance, Caro et al. suggested that the proximity of neighboring boron atoms on average resulted in a significant shift in the energy of the B^+ state.

In this paper, we extend the SCA method to study the addition energy of individual dopants inside a host silicon semiconductor. Using this approach we have observed the behavior of the B^+ state at

the single-acceptor level by both spatially resolving subsurface boron acceptors and detecting spectroscopically single holes entering and leaving these minute systems. This allows us to examine the energy of the B^+ state with respect to the nearest-neighbor distances on an atom-by-atom basis.

Figure 1a shows a schematic of the SCA method and the layout of our experiment. The key component is a sharp metallic tip connected directly to a charge sensor that achieves a sensitivity of $0.01 e/\sqrt{\text{Hz}}$.⁷ We monitor the tip's AC charge q_{tip} in response to an AC excitation voltage V_{exc} applied to an underlying electrode. If the quantum system below the tip can accommodate additional charge, the excitation voltage causes it to resonate between the system and the underlying electrode, giving rise to an enhanced capacitance, $C \equiv q_{\text{tip}}/V_{\text{exc}}$.⁸ To acquire an image, we record the change in C while scanning the tip laterally over a plane with the tip's apex a distance of ~ 1 nm above the silicon surface and with a fixed DC bias voltage V_{tip} . For capacitance spectroscopy, the tip's position is fixed (i.e., not scanned); we then sweep V_{tip} to acquire a C – V curve. For the measurements shown here, we used a chemically etched PtIr tip prepared to have a nanometer-scale radius of curvature of the apex; the data are consistent with a tip radius of less than 25 nm. All data

Received: July 22, 2011

Revised: October 3, 2011

Published: October 24, 2011

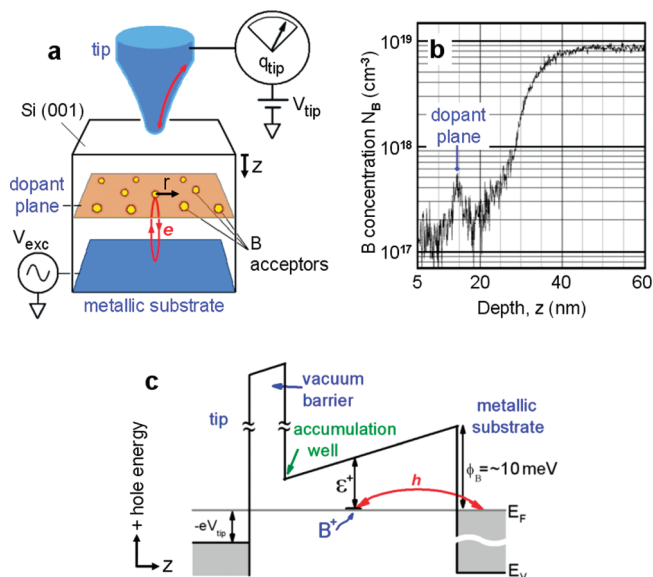


Figure 1. Capacitance-based scanning probe method to detect the charging of boron acceptors in a silicon sample. (a) Schematic of the subsurface charge accumulation method and sample geometry. (b) Secondary ion mass spectroscopy (SIMS) measurement of the boron doping profile of the silicon sample. The top surface corresponds to $z = 0$; SIMS data from $z = 0$ –5 nm exhibit a surface artifact and are not shown. (c) Inverted valence band profile, including the vacuum gap and tip. The red arrow indicates a hole tunneling on and off the B^+ state of a boron acceptor.

were acquired at a temperature of $T = 4.2$ K using the same tip, unless otherwise noted. Tip voltages are reported with respect to the nulling voltage to account for the tip–sample contact potential.⁴

The silicon sample we employed contained a narrow layer of dopants, that is, a “ δ -layer”, 15 nm below the exposed surface. The sample was grown by chemical vapor deposition on a Si(001) substrate, which is similar to the wafer used by Caro et al. The layers consist of (starting from the bottom) p^{+2} Si (500 nm)/ p Si (20 nm)/ δ / p Si (15 nm). Boron is the dopant for the layers and the δ spike. The p^{+2} layer is degenerately doped ($N_B = 10^{19}$ cm⁻³) and serves as the underlying metallic electrode. The lower p layer ($N_B \sim 10^{17}$ cm⁻³) serves as the tunneling barrier, whereas the upper p layer is simply a spacer. The δ spike has areal density of $\rho = 1.7 \times 10^{11}$ cm⁻². Figure 1b shows the doping profile in the structure measured with secondary ion mass spectroscopy. Each of the layers is clearly discernible, with the δ spike appearing as a peak about 2 nm wide and with a maximum concentration of $N_B = 5 \times 10^{17}$ cm⁻³. Further growth details are given in the Supporting Information. Upward B diffusion during growth from the lower degenerately doped layer is responsible for the boron “tail” seen in Figure 1b for z near 20–30 nm. Charging of these tail dopants is expected to result in a negligible measured signal, as discussed in the Supporting Information.

Figure 1c shows the profile of the valence band edge, including the vacuum gap and tip. The tunneling barrier height of ~ 10 meV is formed by the valence band contribution to the bandgap narrowing.⁹ The curved arrow indicates a charge tunneling on and off an acceptor state. For consistency, we will refer to the charges as holes. In reality, the measurement is not sensitive to the sign of the charge carrier; moreover, conceptually a hole entering an acceptor is equivalent to an electron exiting the state.

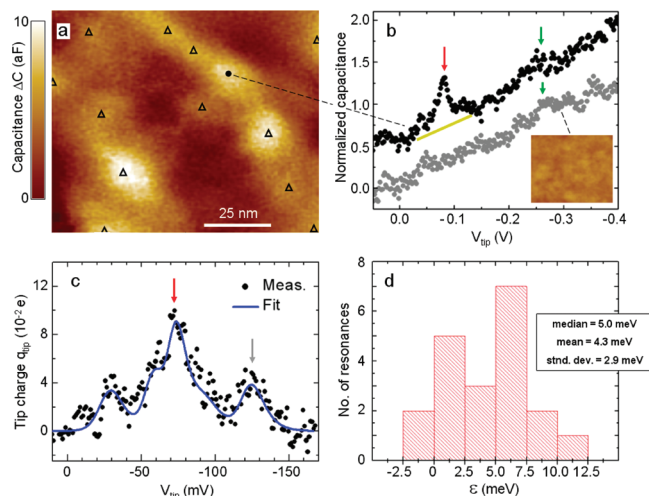


Figure 2. Representative capacitance data. (a) A capacitance image, acquired by fixing the voltage at $V_{tip} = -0.075$ V while scanning. Bright high-capacitance features are clearly resolved. (b) Representative $C-V$ curves. The top curve (black) was acquired at the indicated location of image (a). The bottom curve (gray) was acquired on a different sample that did not contain the δ -layer of dopants. The inset shows a capacitance image of this sample also acquired at the same voltage as (a); the scan range and color scale are also identical to (a). Two types of features were consistently observed in the sample with the δ layer: peaks near $V_{tip} = -0.075$ V (red arrow) and a step near -0.250 V (green arrow). The peaks are consistent with single charges entering the dopant layer; the step is consistent with the formation of an accumulation layer at the sample surface. In contrast, the sample without the δ -layer only shows the step feature. Additional curves and images are shown in the supporting figures. The curves are normalized to the capacitance value at the step feature; for clarity, the top curve is shifted vertically by 0.5 normalized units. (c) Expanded $C-V$ curve showing the peak structure from the top curve in (b) with a background line (yellow) subtracted. The blue solid curve is a fit from a model based on the assumption that each peak corresponds to a single hole entering the system. In this case, the red arrow indicates the primary peak, which we interpret as corresponding to a hole entering a dopant directly below the tip’s apex. Smaller peaks are interpreted as holes entering more distant acceptors. (d) A histogram of the quantum state energies ϵ , extracted from measurements of 20 distinct peaks.

A key parameter is the average spacing between nearest-neighbor dopants. Statistically, nearest-neighbor distances for objects randomly positioned in two-dimensions follow the Poissonian distributions shown in the Supporting Information, Figure S1.¹⁰ For areal density $\rho = 1.7 \times 10^{11}$ cm⁻², the mean distance to the first neighbor is expected to be 12.1 nm. This length is comparable to the 15 nm δ -layer depth, which sets the lower limit to the lateral resolution of the SCA method.¹¹ In other words, the average distance between dopants in our sample is similar to our expected spatial resolution. Hence the goal of resolving the charging of individual subsurface acceptors is within reach.

Figure 2a shows a representative capacitance image. We see well-isolated maxima (bright features) that have a similar intensity. We interpret these as corresponding to individual dopants. Some maxima are larger and likely arise from closely spaced dopants. The triangles and the black dot mark 13 local maxima. To avoid maxima created by nanometer-scale noise, the triangle placement is based on a smoothed image. The smoothed image is shown in Supporting Information Figure S2, which also

includes the surface topography of the Figure 2a area, acquired by using our method in tunneling microscopy mode.⁷ The $1.7 \times 10^{11} \text{ cm}^{-2}$ boron density implies that we should on average observe 14 dopants in an area of this size. This is consistent with the 13 maxima, allowing for the possibility that the especially bright feature in the lower-left portion of Figure 2a arises from two or more closely spaced dopants. Several similar capacitance images were acquired at different locations and we consistently find that the number of bright features approximately agrees with the expected number of boron acceptors using reasonable estimates for the unresolved dopants. Moreover, comparisons to topographical images of the surface show no correlation between the surface topography and the capacitance features. Supporting Information Figure S3 examines the functional form of a bright capacitance feature.

The top (black) data of Figure 2b shows $C-V$ data acquired on a bright feature at the indicated location. The $C-V$ curves on this sample consistently showed the two types of features indicated by the arrows. The green arrow marks a step structure that reproducibly occurred near $V_{\text{tip}} = -0.25 \text{ V}$ with little dependence on the lateral position of the tip. The red arrow indicates a peak structure, which typically was found near $V_{\text{tip}} = -0.075 \text{ V}$. These peaks shifted on the scale of tens of millivolts and often resembled multiple peaks, depending on the location of the probe. For comparison, Supporting Information Figure S4 shows a $C-V$ curve acquired at a location fifteen nanometers from the nearest bright spot. As a control, we also probed a second sample, identical to the sample described above except that it does not contain a δ -layer of boron dopants (a different but identically prepared tip was employed). The results are shown by the bottom (gray) data of Figure 2b. We see that the representative $C-V$ curve is similar but without sharp peaks near $V_{\text{tip}} = -0.075 \text{ V}$. Moreover, capacitance images do not show the distinct maxima, as shown in the inset. Hence we conclude that the sharp peaks in the $C-V$ curves and bright maxima observed in capacitance images correspond to subsurface B dopants in the δ -layer.

The step structure likely results from the accumulation of charge in the surface potential well indicated in Figure 1c (green arrow). Although a detailed description of the formation of this layer is complicated by the fringing nature of the tip's electric field, we can estimate the threshold potential using a parallel-plate picture. The first charge will enter the surface accumulation layer at a tip potential of $V_{\text{tip}}^{\text{step}} = (\phi_{\text{B}} + \Delta)/\alpha e$, where e is the elementary charge, Δ is the quantum level spacing between the bottom of the well and the first hole state to appear, and α is the voltage lever-arm that scales the applied voltage to account for the potential drop between the tip and the layer of interest within the sample. We expect approximately $\alpha = 0.2$ directly below the apex,¹² and $\phi_{\text{B}} = 11.7 \text{ meV}$.⁶ With regard to Δ , the accumulation layer will initially form a quantum dot below the apex of the tip of radius $\sim 25 \text{ nm}$, determined mostly by the tip radius. From a simple estimate based on a quantum box of this size, and using a hole effective mass of half of the free electron mass, we find approximately $\Delta = 10 \text{ meV}$. These values give $V_{\text{tip}}^{\text{step}} = 100 \text{ mV}$. As V_{tip} increase further, the dot will grow in size and more charges will enter. As a result, a conducting surface layer is expected to form giving rise to the characteristic step-like $C-V$ curve.⁴

To analyze the peak structure (red arrow), we consider a quantum state of energy ε of a dopant that is a distance z below the surface and laterally displaced from the tip's apex by r

(see Figure 1a). We again start from the parallel-plate expression for the resonance tip voltage for this state

$$V_{\text{tip}}^{\text{peak}} = \frac{\phi_{\text{B}} - \varepsilon}{\alpha(z,r)e} \quad (1)$$

Here, in contrast to the expression for $V_{\text{tip}}^{\text{step}}$ we have generalized the lever arm to account approximately for the fringing pattern of electric field between the tip and sample. Essentially, a dopant a few nanometers below the surface and directly below the tip, $r = 0$, has a larger lever arm than a deeper and laterally displaced dopant. We account for this by allowing the parameter to be a function of z and r . Of course $\alpha(z,r)$ also depends on the distance between the tip and surface, which is $\sim 1 \text{ nm}$; this variation can be effectively absorbed into z . A detailed analysis of the electrostatics of the tip-sample system is given in ref 11.

Figure 2c redisplay the $C-V$ data with a linear background subtraction (gray line in Figure 2b) and an expanded voltage scale. The solid curve shows a calculated fit based on single-electron capacitance peaks, which are essentially the convolution of semielliptical peaks with the derivative of the Fermi function.¹² As detailed in Methods in Supporting Information, the fitting procedure superposes 4–6 single-electron peaks and invokes two free parameters for each peak, $\alpha(z,r)$ and $V_{\text{tip}}^{\text{peak}}$, which are varied to achieve the best fit. Essentially, the peak height must equal $e\alpha(z,r)$ due to the quantization of charge,¹² allowing us to do a case-by-case estimate of the lever arm. We see that this procedure reproduces the measured curve well. We define the primary peak as the peak with the largest $\alpha(z,r)$, which we interpret as arising from charge entering an acceptor directly below the tip's apex; whereas the other peaks, which we designate as secondary peaks, correspond to the charging of more distant dopants with respect to the tip position.

To extract the values of ε from our data, we apply eq 1 using the measured $V_{\text{tip}}^{\text{peak}}$ values and the $\alpha(z,r)$ parameters determined for each peak by the above fitting procedure. These measurements were reproducible over time scales of several hours and we estimate the uncertainty of the extracted ε values to be $\pm 1 \text{ meV}$, as shown in Supporting Information Figure S5. For the primary peak shown in Figure 2c, the lever arm was determined to be $\alpha(z,0) = 0.156$ and the extracted energy from eq 1 was $\varepsilon = 0.2 \text{ meV}$. By probing different areas on the sample, we have observed 20 peaks of sufficient quality to apply this procedure. Figure 2d shows the resulting histogram of the extracted energies, which have a mean value of $4.3 \pm 2.9 \text{ meV}$, where the uncertainty was determined by the standard deviation. The mean value compares well to the average B^+ energies of 6.7 meV observed for a similar sample by Caro and co-workers. With regard to the width of the distribution, the $\sim 3 \text{ meV}$ standard deviation is about three times greater than was observed by Caro et al. We believe the discrepancy is because the electrostatic environment of the boron dopants is different for the two experiments. For the ref 6 sample configuration, the dopant plane was sandwiched between two thick layers of degenerately doped silicon. For the sample configuration of this work, effectively one of these layers is missing so that the dopant plane is 15 nm away from an exposed silicon surface with an ambient oxide layer. It is likely that electrons and holes trapped in the oxide layer contribute the additional variance to the B^+ energies. To be clear, we believe this additional disorder is electrostatic in origin and not a confinement effect of the nearby surface.

In light of both the $C-V$ curve and capacitance image data, we conclude that we are observing the B^+ state of individual boron dopants; the peaks in the $C-V$ curves correspond to the energies (ε^+) and the imaged high-capacitance bright spots mark the locations of the acceptors.

To examine the effects of interactions of neighboring acceptors, we consider the secondary peaks more carefully. As shown in ref 11, the lever arm for a subsurface dopant displaced from the tip's apex by r is proportional to the Lorentzian $[1 + (r/w)^2]^{-1}$, where w is approximately equal to the depth of the underlying conducting layer, which is 35 nm for our sample. If we assume that the primary peak arises from a dopant directly below the apex, we can normalize the Lorentzian with respect to corresponding lever arm, $\alpha_p = \alpha(z,0)$. Moreover, if we assume that for a given curve the primary and secondary dopants lie in the same horizontal plane, we can neglect the z -dependence. Hence, we can express approximately the r -dependence of the lever arm for the secondary dopants $\alpha_s(r)$ as

$$\frac{\alpha_s(r)}{\alpha_p} = \left[1 + \left(\frac{r}{35 \text{ nm}} \right)^2 \right]^{-1} \quad (2)$$

Returning to Figure 2c, consider the secondary peak marked by the gray arrow. For this peak, the best-fit lever arm is 0.097; thus $\alpha_s/\alpha_p = 0.097/0.156 = 0.622$. Applying eq 2, we assert that this dopant was approximately a distance of $r = 27$ nm from the primary dopant. Supporting Information Figure S6 presents a table that shows the lever-arm parameters and the extracted distances of secondary dopants for all of the Figure 2c peaks (and a similar analysis for data acquired at a nearby location). These distances compare well to the spacings of the bright features in the images; the comparison allows us to estimate the uncertainty for extracting distances in this way.

The resonant tunneling spectroscopy experiment by Caro et al. suggested that the proximity of neighboring acceptors resulted in a shift of the average B^+ binding energy to 6.7 meV, instead of the expected 2.0 meV.⁶ Our method allows us to directly investigate the effect of neighboring dopants; we do this by examining the measured ε^+ of a particular primary peak versus the distance to its nearest neighbor, R , based on the analysis of secondary peaks.

We have obtained sufficiently high-quality data to extract ε^+ and R values for six measurements. The results are shown in Figure 3. We see that for three of the data sets the nearest-neighbor distance was less than 12 nm (the expected mean distance) and for two of the data sets R was greater than 12 nm. The plot shows that acceptors with closer nearest neighbors tend to have greater binding energies for the second hole. This trend is consistent with the interpretation of the resonant tunneling spectroscopy experiment. Figures 2d and 3 highlight the innovation of our scanning probe experiment. In contrast to most transport measurements which find the average behavior of many dopants, millions in the case of ref 5, we are able to discern both the average and the atom-by-atom binding energies.

To explore theoretically the effect of neighboring dopants on the B^+ state, we have calculated the energy to add a third hole to a system of two neutral acceptors separated by a distance R . The calculations were performed using the configuration-interaction method^{13,14} in the context of the effective-mass theory.^{15,16} In this approximation, an acceptor is regarded as a hydrogenic atom with an effective Rydberg energy Ry^* and Bohr radius a_0^* . Both of the effective parameters are defined with respect to the first hole

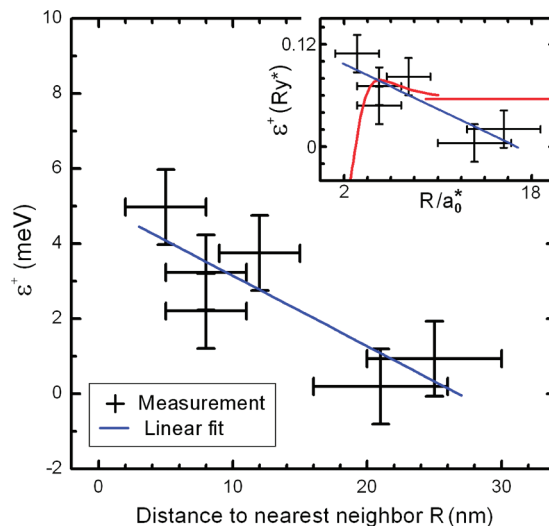


Figure 3. Hole binding energy versus nearest-neighbor distance. The main plot shows primary-peak binding energy plotted as a function of nearest-neighbor distance R . The parameters were extracted from measurements of dopants at different locations, including the data shown in Figure 2c. Shown in blue is a least-squares linear fit. The error bars show the estimated uncertainty of the energy and distance; details of these estimates are given in Supporting Information, Figures S5 and S6. The inset shows the data replotted with respect to the effective Rydberg energy and Bohr radius and compared to a hydrogenic model (red). The model incorporates two neutral acceptors and finds the binding energy of a third-hole; ε^+ is positive if the third charge results in a lower electronic energy for the system, that is, if the third hole is bound. For $R/a_0^* > 9$ in place of the calculation, we show the asymptotic solution of ε^+ , which equals the solution for an isolated acceptor.¹⁶

of an isolated acceptor: Ry^* is equal to the binding energy and a_0^* is equal to the average radius of the wave function. For boron in silicon $Ry^* = 45.7$ meV, and we estimate $a_0^* = 1.6$ nm, following ref 5. Figure 3 (inset) shows the calculated third-hole binding energy in red. For self-consistency, we retain the notation ε^+ for the energy of this state; however the hole is clearly interacting with both dopants, as discussed below. For $R > 9a_0^*$, we show the asymptotic solution of ε^+ , which equals that of an isolated acceptor with two holes.¹⁷ We see that ε^+ is predicted to be positive for separations $R > 3a_0$, indicating that the third hole is bound. In the range of separations $5a_0^* < R < 16a_0^*$, we see that the calculated curve has a small negative slope. Our data are consistent with this trend, and qualitatively consistent with the resonant tunneling measurements. However the data show greater-than-predicted slope compared to our model. Moreover, the calculation shows the opposite trend at small R with a maximum near $R = 5a_0^*$, which is not apparent in the measured data.

The behavior for large separations, $R > 5a_0^*$, can be understood as a consequence of basic quantum-mechanics of molecules. Consider $R \gg 10a_0^*$ in which case each B^0 is effectively isolated; here it is well established that an additional hole experiences a weak attraction to each neutral acceptor due to polarization. Hence either one can bind the third hole and form the B^+ state. This state is analogous to hydrogen-minus, a proton with two bound electrons. For the isolated B^+ state the size of the wave function is rather large as the root-mean-square distance of the hole to the acceptor is $r^* = 5.8a_0^*$.⁶ If we now allow the two neutral acceptors to be separated by $R \sim 10a_0^*$, the third hole has some reasonable probability to be found at either location. Hence, the corresponding wave function resembles a

molecule with two peaks centered on each atom, each peak with a width $\sim r^*$. As the acceptor distance decreases the gradient of the wave function decreases along the line connecting the two atoms. The effect decreases the energy of the state, which increases the binding energy of the third hole. At sufficiently close separations, this behavior will break down as the system will be poorly described as a two-acceptor molecule, instead behaving more as a single atom.¹⁸ Our calculations show that this crossover should occur for $R \cong 5a_0^*$, where ε^+ exhibits the maximum. In other words, our model predicts that the B^+ binding energy will first increase and then decrease with R , behavior that is not seen in the experiment.

The level of agreement between our measurements and calculated curve is not surprising in light of the highly simplified nature of the theoretical model, which incorporates only one neighbor and neglects effects arising from the semiconductor host such as the periodic crystalline potential. We expect the effects of the host crystal to become more pronounced for dopants separated by less than a few nanometers, in which case R becomes comparable to several lattice constants. In other words, at such small distances, simple models such as ours can at best generate trends; more atomistic calculations would be required to test for and compare to the monotonic behavior with respect to dopant separation observed in our experiment.

To the best of our knowledge, at present there is no complete theory for the binding energy of the third hole (or electron) as a function of separation for a semiconductor dopant pair. However, recent calculations by the Das Sarma group focusing on one electron bound to closely spaced pairs of P donors in Si predict that the precise separation and orientation of the dopant pair with respect to the crystalline axes are crucial parameters in determining the ground state wave functions.^{19,20} Although the ground state wave functions in silicon for holes bound to donors are clearly very different, detailed calculations for boron acceptors may yield similarly surprising effects.

■ ASSOCIATED CONTENT

S Supporting Information. Detailed descriptions of the sample preparation, the measurement and analysis methods, the statistical distances to neighboring dopants, the functional form of an imaged dopant, the reproducibility of $C-V$ curves, estimates of energy uncertainty, and nearest-neighbor-distance uncertainty. This material is available free of charge via the Internet at <http://pubs.acs.org>.

■ AUTHOR INFORMATION

Corresponding Author

*E-mail: tessmer@msu.edu.

Present Addresses

[#]Department of Physics, Mercyhurst College, Erie, Pennsylvania 16546, United States.

■ ACKNOWLEDGMENT

We gratefully acknowledge assistance with sample growth by Dirk Rondas and sample characterization by Wilfried Vandervorst. We gained valuable insight from conversations with C. Piermarocchi, T. A. Kaplan, M. I. Dykman, B. Golding, C. Kayis, I. Kuljanishvili, S. D. Mahanti, and M. Y. Simmons. This work was

supported by the Michigan State Institute for Quantum Sciences, the Nation Science Foundation, DMR-0305461, DMR-0906939, the Dutch Organization for Fundamental Research on Matter (FOM), and the European Community's seventh Framework under the Grant Agreements nr:214989-AFSiD and nr:215750-MOLOC.

■ REFERENCES

- (1) Lansbergen, G. P.; Rahman, R.; Wellard, C. J.; Woo, I.; Caro, J.; Collaert, N.; Biesemans, S.; Klimeck, G.; Hollenberg, L. C. L.; Rogge, S. *Nat. Phys.* **2008**, *4*, 656–661.
- (2) Ruess, F. J.; Pok, W.; Reusch, T. C. G.; Butcher, M. J.; Goh, K. E. J.; Oberbeck, L.; Scappucci, G.; Hamilton, A. R.; Simmons, M. Y. *Small* **2007**, *3*, 563–567.
- (3) Teichmann, K.; Wenderoth, M.; Loth, S.; Garleff, J. K.; Wijnheijmer, A. P.; Koenraad, P. M.; Ulbrich, R. G. *Nano Lett.* **2011**, *11* (9), 3538–3542.
- (4) Kuljanishvili, I.; Kayis, C.; Harrison, J. F.; Piermarocchi, C.; Kaplan, T. A.; Tessmer, S. H.; Pfeiffer, L. N.; West, K. W. *Nat. Phys.* **2008**, *4*, 227–233.
- (5) Tessmer, S. H.; Glicofridis, P. I.; Ashoori, R. C.; Levitov, L. S.; Melloch, M. R. *Nature* **1998**, *392*, 51–54.
- (6) Caro, J.; Vink, I. D.; Smit, G. D. J.; Rogge, S.; Klapwijk, T. M.; Loo, R.; Caymax, M. *Phys. Rev. B* **2004**, *69*, 125324.
- (7) Urazhdin, S.; Maasilta, I. J.; Chakraborty, S.; Moraru, I.; Tessmer, S. H. *Rev. Sci. Instrum.* **2000**, *71*, 4170–4173.
- (8) Kaplan, T. A. *J. Stat. Phys.* **2006**, *122*, 1237–1260.
- (9) Yuan, H. X.; Perera, A. G. U. *J. Appl. Phys.* **1996**, *79*, 4418–4425.
- (10) Tessmer, S. H.; Kuljanishvili, I.; Kayis, C.; Harrison, J. F.; Piermarocchi, C.; Kaplan, T. A. *Physica B* **2008**, *403*, 3774–3780.
- (11) Kuljanishvili, I.; Chakraborty, S.; Maasilta, I. J.; Tessmer, S. H. *Ultramicroscopy* **2004**, *102*, 7–12.
- (12) Tessmer, S. H.; Kuljanishvili, I. *Nanotechnology* **2008**, *19*, 445503.
- (13) Slater, J. C. *Quantum Theory of Molecules and Solids. Electronic Structure of Molecules*; McGraw-Hill: New York, 1963; Vol. 1.
- (14) Dunning, T. H. *J. Chem. Phys.* **1989**, *90*, 1007–1023.
- (15) Kohn, W.; Luttinger, J. M. *Phys. Rev.* **1955**, *98*, 915–922.
- (16) Davies, J. H. *The Physics of Low-dimensional Semiconductors: An Introduction*; Cambridge University Press: Cambridge, 1998.
- (17) Phelps, D. E.; Bajaj, K. K. *Astrophys. J.* **1983**, *268*, 447–450.
- (18) For $R = 0$, the system is analogous to the helium atom, for which the third electron (He^-) is not bound in the lowest state corresponding to the configuration $1s^2 2s$. For a thorough review, see: Buckman, S. J.; Clark, C. W. *Rev. Mod. Phys.* **1994**, *66*, 539–655.
- (19) Koiller, B.; Hu, X. D.; Das Sarma, S. *Phys. Rev. B* **2006**, *73*, 045319.
- (20) Hu, X. D.; Koiller, B.; Das Sarma, S. *Phys. Rev. B* **2005**, *71*, 235332.